Characterization and testing of a new environmental chamber

A. Leskinen[1,2], P. Yli-Pirilä[2], K. Kuuspalo[3], O. Sippula[3], P. Jalava[3], M.-R. Hirvonen[3], J. Jokiniemi[3], A. Virtanen[2], M. Komppula[1], and K. E. J. Lehtinen[1,2]

[1]Finnish Meteorological Institute, P. O. Box 1627, 70211 Kuopio, Finland
[2]University of Eastern Finland, Department of Applied Physics, P. O. Box 1627, 70211 Kuopio, Finland
[3]University of Eastern Finland, Department of Environmental Science, P. O. Box 1627, 70211 Kuopio, Finland

Correspondence to: A. Leskinen (ari.leskinen@fmi.fi)

Abstract. A $29\,m^3$ Teflon chamber, designed for studies on the aging of combustion aerosols, at the University of Eastern Finland is described and characterized. The chamber is part of a research facility, called Ilmari, where small-scale combustion devices, a dynamometer for vehicle exhaust studies, dilution systems, the chamber, and cell and animal exposure devices are located side by side under the same roof. The small surface-to-volume ratio of the chamber enables reasonably long experiment times, with particle wall loss rate constants of 0.088, 0.080, 0.045, and $0.040\,h^{-1}$ for polydisperse, 50, 100, and 200 nm monodisperse aerosols, respectively. The NO_2 photolysis rate can be adjusted from 0 to $0.62\,min^{-1}$. The irradiance spectrum is centered at either 350 or 365 nm, and the maximum irradiance, produced by up to 160 blacklight lamps, is $29.7\,W\,m^{-2}$, which corresponds to the ultraviolet (UV) irradiance in Central Finland at noon on a sunny day in the midsummer. The temperature inside the chamber is uniform and can be kept at $25 \pm 1\,°C$. The chamber is kept in an overpressure with a moving top frame, which reduces sample dilution and entrance of contamination during an experiment. The functionality of the chamber was tested with oxidation experiments of toluene, resulting in secondary organic aerosol (SOA) yields of 12–42 %, depending on the initial conditions, such as NO_x concentration and UV irradiation. The highest gaseous oxidation product yields of 12.4–19.5 % and 5.8–19.5 % were detected with ions corresponding to methyl glyoxal (m/z 73.029) and 4-oxo-2-pentenal (m/z 99.044), respectively. Overall, reasonable yields of SOA and gaseous reaction products, comparable to those obtained in other laboratories, were obtained.

1 Introduction

Atmospheric aerosols undergo changes in their physico-chemical properties, such as size and chemical composition, during their residence in the atmosphere. These changes are due to aerosol dynamic processes – such as coagulation, condensation, and evaporation – and photochemical reactions with atmospheric oxidants. During aging a substantial amount of secondary organic aerosol (SOA) is formed, which is further oxidized with increasing aging time (e.g., Ziemann and Atkinson, 2012; Hallquist et al., 2009). This may lead to significant changes, e.g., in the health- and climate-relevant properties of atmospheric aerosols.

Atmospheric transformation processes have been studied extensively and for decades in environmental chambers with different designs (e.g., Wang et al., 2014; Platt et al., 2013; Carter et al., 2005; Paulsen et al., 2005; Cocker et al., 2001). The most used chamber materials are glass, stainless steel, and Teflon. Glass and stainless-steel walls are rigid so such chambers have a fixed volume, whereas a thin heat-sealable Teflon film enables the construction of a collapsible bag, whose volume decreases as sample is taken out. Teflon is also advantageous, because it is inert and withstands the mechanical stress when the chamber frequently collapses and expands.

Rigid walls are advantageous in experiments which are carried out at a pressure that is much different from the ambient pressure. However, when a sample is taken out, the aerosol in the chamber dilutes, which affects, e.g., the reaction rates in the chamber. In collapsible bags, sampling does not dilute the aerosol unless there are inward leaks through the walls. This can be prevented by keeping the bag at a slight

overpressure, so the flow through the possible cracks is rather outwards than inwards.

When photochemical reactions are to be studied, the chamber material must let through the relevant ultraviolet irradiation, such as sunlight in outdoor chambers or artificial lights in indoor chambers. For Teflon films the penetration is high, whereas for glass, excluding quartz glass, the penetration is weaker.

In addition to chambers, the aging processes due to oxidation can be studied in flow reactors (e.g., Keller and Burtscher, 2012; Lambe et al., 2011), where the aerosol is aged fast in an environment with a high concentration of oxidants. This enables achieving chamber-equivalent photochemical age of several hours in seconds. The short residence time reduces wall losses, although the transition efficiency, especially for nanoparticles, is low, which is a considerable characteristic if new particle formation is studied (Keller and Burtscher, 2012). Another advantage of a flow reactor is its relatively small size and portability. Environmental chambers can, however, also be mobile, such as the one described by Platt et al. (2013), and can be brought close to emission sources, such as vegetation, stacks, or tailpipes.

The chambers and flow reactors offer, in general, convenient and fairly inexpensive ways to investigate the properties of an aging aerosol, compared to, e.g., aircraft or balloon measurements along the trajectory of an air parcel in the atmosphere. Furthermore, conditions such as temperature; humidity, and composition of the parent aerosol, precursors, and oxidants in the chamber can be controlled. One drawback of an environmental chamber, compared to atmospheric measurements, is that the chamber walls act as a sink for the studied aerosol, as a part of the aerosol particles and gaseous compounds are lost to the chamber walls due to deposition and chemical reactions (e.g., McMurry and Grosjean, 1985). The effect of wall losses on the experimental results can, however, be taken into account afterwards in data analysis, but the losses limit experiment duration. Contaminants can also penetrate through the walls into the chamber, or the species deposited on the walls in previous experiments may be released. Therefore, the chamber must be cleaned as well as possible between the experiments.

In this paper, the environmental chamber at Ilmari, an online aerosol exposure unit at the University of Eastern Finland, is described for the first time. The technical details of the chamber are given and discussed. In Ilmari the main scientific focus is to study the toxicological effects of both fresh primary and aged, combustion-derived aerosols. The emission sources, the chamber, and the exposure units are side by side under the same roof, which is an advantage due to relatively short transport lines.

Results from first test runs with a mixture of toluene, ozone, and nitrous acid (HONO), serving as a hydroxyl (OH) radical precursor, under the influence of UV radiation from blacklights, are presented and discussed, in order to test the functionality of the chamber for SOA formation studies.
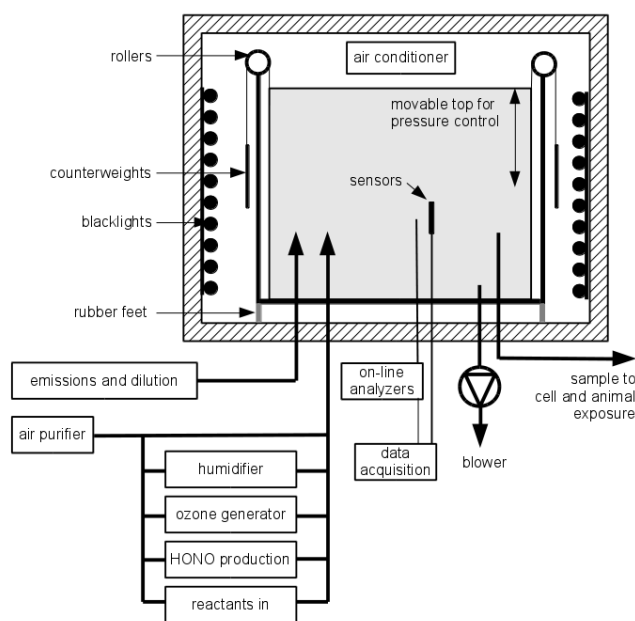

Figure 1. The schematics of the Ilmari chamber facilities.

2 Methods

2.1 The environmental chamber

The chamber, sketched in Fig. 1, is manufactured by Foiltec GmbH, Germany, of a 125 μm thick fluorinated ethylene propylene resin (Teflon® FEP). Its shape is a rectangular prism and it measures 3.5 m (length) × 3.5 m (width) × 2.4 m (height). Thus, its nominal volume and surface area are, when full, 29.4 m³ and 58.1 m², respectively. The surface-to-volume ratio for a chamber is a parameter that describes, for example, the degree of wall effects. The higher the ratio, the more frequently the aerosol contacts the walls. For example, values of 3.0 in a 8 m³ chamber and of 1.4 in a 90 m³ chamber have been reported (Platt et al., 2013; Carter et al., 2005). In our chamber the surface-to-volume ratio is 2.0, which is equal to the surface-to-volume ratio of several other 27–30 m³ chambers (Wang et al., 2014; Paulsen et al., 2005; Cocker et al., 2001).

The chamber is a collapsible bag, which is attached to a moving top frame. There are counterweights attached to the top frame by a steel wire, which goes over four low-friction rollers. The rollers are attached to the supporting frame around the chamber. All frames are made of an aluminium profile, whose cross section is 30 mm × 30 mm. The chamber is electrically insulated from the surroundings by letting the framework stand on rubber feet and by preventing the chamber walls from touching the surrounding objects.

The pressure inside the chamber can be controlled by adding or removing extra weights on the moving top frame. In normal operation the combined weight of the chamber bag, the moving frame, and the extra weights is slightly more
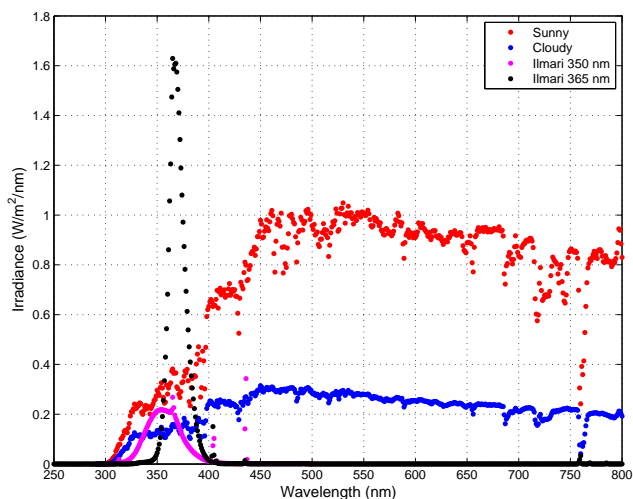
Figure 2. The spectral irradiance of the 350 and 365 nm blacklight lamps at Ilmari and those measured at ground level in Kuopio at noon in July in sunny and cloudy weather.

than that of the counterweights, so the top frame pushes the chamber bag and maintains an overpressure in the chamber. The typical overpressure inside the chamber is around 10 Pa when the chamber is full. The overpressure decreases when a sample is taken out of the chamber, because the weight of the chamber is increasingly supported by the bottom grid as the chamber is collapsed. The pressure difference between the chamber and the surroundings (the experimental hall) is measured by a MicaFlex MF-PD pressure difference sensor (Mikor Instuments Ltd., Finland), whose operating range is -50 to 50 Pa with an accuracy of ± 1.0 Pa.

Two arrays of blacklight lamps (Sylvania F36/T8 BLB 36 W or Sylvania F 40 W/350 BL) are placed between the enclosure wall and the chamber, on two opposite sides. The blacklight lamps irradiate a spectrum that is centered at 365 nm (the Sylvania F36/T8 BLB 36 W lamps, denoted hereafter as "365 nm lamps") or at 350 nm (the Sylvania F 40 W/350 BL lamps, denoted hereafter as "350 nm lamps") with half-widths of 16 nm (Fig. 2).

The blacklight lamps can be switched on in 18 different combination, thereby enabling the adjustment of the output irradiance in almost a continuous manner. The inner walls of the enclosure are covered by aluminium plates (floor) or foil (walls and ceiling) in order to enhance and equalize the UV radiation. The spectral irradiance inside the enclosure was measured with a portable spectroradiometer (Optronic OL756), equipped with a dome window for semi-spatial irradiance measurements. The measured wavelength range was 250 to 800 nm with a bandwidth of 1 nm. The total irradiance was calculated by integrating the spectral irradiance over the measured wavelength range.

The chamber is located in a thermally insulated enclosure, whose inner dimensions are 4.3 m (width) $\times$ 4.6 m (length)

$\times$ 3.1 m (height). The temperature of the enclosure is controlled by a thermostated air conditioner (Argo AW 764 CL3), with a maximum cooling power of 6.5 kW. The desired temperature can be preset in the range of 16 to 25 °C. The temperature in the chamber is measured at nine points in order to monitor possible temperature gradients in the chamber. In the middle of the chamber there is a combined temperature and humidity probe (Vaisala HMP 60; -40 to 60 °C and 0–100 % RH) and a diffusion type carbon dioxide (CO_2) sensor (Vaisala GMP 343; 0–1000 ppm). Near each corner (20 cm from the corner) there are altogether eight K-type thermocouples.

The inlet and outlet ports (Swagelok®) are attached to an aluminium plate (diameter 0.5 m, thickness 5 mm), whose inner surface is covered by a Teflon film, in the bottom face of the chamber. Stainless-steel sampling lines having 6, 10, and 25 mm outer diameter are attached to the ports. The ends of the lines are at 1.0 m height from the chamber bottom (inside the chamber) and 0.5 m below the chamber (outside). Manual control valves are used to open and close separate lines. Maintenance work inside the chamber is possible when a 0.5 m $\times$ 0.5 m aluminium plate in the bottom face is removed.

The data from the sensors are acquired by National Instrument DAQ modules (NI9207 and NI9213) and transferred wirelessly to a PC, where they are stored in a database with a time resolution of 1 s by using a Datain data fusion system (Kuava Ltd., Finland).

2.2 Characterization of the chamber

2.2.1 Aerosol wall losses

Ammonium sulfate (($NH_4)_2SO_4$) particles were produced from a $1\,g\,L^{-1}$ solution of ($NH_4)_2SO_4$ in water by using a constant output atomizer (TSI 3076), a silica gel diffusion dryer, and a Kr-85 bipolar diffusion charger. The neutralized aerosol was injected directly into the chamber, filled with purified air, either as a polydisperse sample (for 30 min at a flow rate of $3.0\,L\,min^{-1}$) or through a size-selective differential mobility analyzer (TSI 3081 DMA) as monodisperse samples (for 2 h at the flow rate of $1.9\,L\,min^{-1}$). The number median diameter and geometric standard deviation of the polydisperse samples were 70 nm and 1.8, respectively, and the mobility equivalent diameters of the monodisperse samples were 50, 100, and 200 nm. It must be noted that a fraction of the particles exiting the DMA are larger than the selected size, possessing multiple elementary charges and therefore the same electrical mobility. The fraction of the multiply charged particles is estimated to be 4 % for the 50 nm, 14 % for the 100 nm, and 27 % for the 200 nm monodisperse aerosol (Wiedensohler, 1988). The number concentration of the multiply charged particles was subtracted from the total number concentration of the monodisperse samples in the aerosol wall loss analysis.

The particle size distribution (14–750 nm) in the chamber was monitored, during the injection and the experiments that lasted 13–24 h, with a scanning mobility particle sizer (SMPS; TSI 3081 DMA + 3775 CPC) with a time resolution of 5 min. The total particle number concentration was obtained by integrating the size distribution over the particle size.

Provided that the aerosol in the chamber is well mixed, a coefficient for the wall loss rate, β_i (s^{-1}), can be defined from (Crump et al., 1983)

$$dN_i/dt = -\beta_i N_i, \tag{1}$$

where N_i is the number concentration (cm^{-3}) of particles of size class i in the chamber. The coefficient β_i for each size class was obtained by integrating Eq. (1), which gives $-\ln(N_i/N_{i,0}) = \beta_i t$, and then by performing a linear fit to the data $(t, \ln(N_i/N_{i,0}))$, where $N_{i,0}$ is the initial number concentration (cm^{-3}) of size class i.

2.2.2 NO$_2$ photolysis rate

The photolysis rate of nitrogen dioxide (j_{NO_2}) was determined in order to characterize the photochemical potential of the 365 nm blacklights for the cases when 54 (one-third of all), 108 (two-thirds of all), or 160 (all) lamps were switched on. For the 350 nm blacklights j_{NO_2} was determined with 47 (all) lamps on. NO$_2$, NO, and O$_3$ concentrations in the chamber were monitored with a trace-level chemiluminescence NO–NO$_2$–NO$_x$ analyzer (Thermo 42i-TL) and a UV photometric ozone analyzer (Thermo 49i). NO$_2$ was injected from a gas cylinder into the chamber which had been flushed with purified air, produced from indoor air with an oil-free compressor with a ballast tank and an air purifier with methane reactors (Model 737–250, Aadco Instruments Inc., USA). The system produces air with less than 1 ppb of ozone, methane, hydrocarbons, NO, NO$_x$, H$_2$S, SO$_2$, COS, CO, CO$_2$, SF$_6$, and fluorocarbons at a nominal flow rate of 250 L min^{-1}. After 5 min for equilibration, all blacklights were switched on. The photolysis of NO$_2$ leads to formation of NO and O$_3$, which in turn react with each other, producing NO$_2$, and after some time an equilibrium is established. The NO$_2$ photolysis rate can be calculated from the equilibrium concentrations [NO] (molecule cm^{-3}), [O$_3$] (molecule cm^{-3}), and [NO$_2$] (molecule cm^{-3}) as

$$j_{NO_2} = k[NO][O_3]/[NO_2], \tag{2}$$

where $k = 1.8 \times 10^{-14}$ cm^3 molecule^{-1} s^{-1} is the rate constant of the reaction between O$_3$ and NO at 298 K (Seinfeld and Pandis, 2006). Similar equilibria were sought for the cases when only two-thirds or one-third of the lamps were switched on, in order to find out the effect of irradiance on the NO$_2$ photolysis rate. Since the equilibrium holds only in the presence of the UV lights, the gas concentrations start changing immediately when they enter the dark sampling line to the gas analyzers. In our case, the residence time between the chamber and the analyzers was 0.8 s, and therefore the gas concentrations were corrected based on the reaction between O$_3$ and NO.

2.2.3 Inter-experiment cleaning of the chamber

The following procedure was used to clean the chamber when conducting the first experiments in 2013. First, the aerosol from the chamber was sucked fast by the help of a blower until the chamber collapsed (pressure difference −5 Pa). Then the chamber was filled with purified and ozonized air with a high humidity (> 90 % RH). Dry, purified air was conditioned with a Model FC125-240-5MP-02 (Perma Pure LLC., USA) humidifier, where the humidity of the air flowing through is controlled by the temperature of the deionized water on the other side of 240 pieces of Nafion® membrane tubes which allow water molecules to pass from the water stream into the air flow. During the filling stage of the chamber cleaning the water temperature in the humidifier was 35 °C. The ozone was generated by irradiating (at 185 nm wavelength) a part of the dry, purified air with a high-energy UV lamp , filtered with a high-efficiency particulate absorption (HEPA) filter and mixed with the humid air before transporting into the chamber. The temperature, relative humidity (RH), overpressure, and ozone concentration in the chamber were monitored with the instruments described in Sects. 2.1 and 2.2.2, and necessary adjustments were made in order to keep the RH above 90 % and ozone concentration above 1 ppm. When the chamber reached its full volume, an outlet port was opened and all blacklight lamps were switched on in order to "bake" the chamber walls and to remove the impurities from the chamber. The baking and flushing phase was continued for 2 h, after which all blacklights and ozone generation were switched off and the chamber was flushed overnight with purified air, whose relative humidity was set to about 50 %, the value to be used in the next experiment. A similar procedure was used by Platt et al. (2013) in their mobile environmental chamber. It must be noted that the high humidity we used may have caused condensation in some local cold spots on the chamber walls. However, since the high humidity was used only in the beginning of the cleaning process, we estimate that during the overnight flushing of at least 12 h with drier air the possibly condensed water evaporated from the walls.

In the latter characterization experiments in 2014–2015 the chamber was cleaned by sucking the air from the chamber and then filling the chamber with purified air and flushing overnight. In order to determine the background particle formation, we irradiated pure air or a mixture of pure air and carbon monoxide (CO) for 4 h and monitored the particle number concentration and size distribution in the chamber. The background particle formation is due to either particle or particle precursor contamination, originating from the pure air source or the chamber walls. By adding CO, we could see

if the contamination is due to particle precursors, because CO suppresses OH radicals and SOA formation.

2.3 Test runs with toluene, ozone, and OH radicals under the influence of UV

Altogether seven experiments with toluene (C_7H_8) in the presence of OH radicals under the influence of the blacklights were carried out. Four experiments (T130909–T130912) were carried out without seed particles, and three experiments (T150113, T150114, and T150120) with sodium chloride (NaCl) seed particles. The seed particles were produced by nebulizing a solution of NaCl (1 wt %) with an atomizer (Topas ATM 226). The produced particles were dried in a silica gel diffusion dryer and injected into the chamber. After a short stabilization time, HONO was produced by titrating sodium nitrite ($NaNO_2$) solution (1 wt %) into sulfuric acid (H_2SO_4) solution (10 wt %) in a glass flask equipped with a magnetic stirrer, based on the method developed by Taira and Kanda (1990). The gaseous HONO was carried by a purified air flow of $3.0 \, L \, min^{-1}$ into the chamber. The HONO concentration, and the consequential OH radical concentration, in the chamber was adjusted by the amount of the $NaNO_2$ and the injection time. The mixing of HONO was monitored from the NO_2 concentration calculated by the NO–NO_x analyzer as the difference between NO_x and NO concentrations, because the instrument reduces HONO to NO in a similar manner to the conversion of NO_2 (Taira and Kanda, 1990). The titration also produces NO and NO_2, whose concentrations depend on the carrier gas flow rate. At the flow rate of $3.0 \, L \, min^{-1}$ in our experiments, however, the fractions of NO and NO_2 can be considered negligible (Taira and Kanda, 1990).

When the HONO concentration in the chamber had stabilized, we injected ozone into the chamber (ozone generation is described in Sect. 2.2.3) in some experiments until a desired concentration was achieved. We used ozone to convert the NO, produced in HONO generation, to NO_2 in order to start the photochemistry initiated by NO_2 dissociation as soon as possible after turning the lights on. We strove for an initial ozone concentration of about 30 ppb, a comparable concentration to the lower atmosphere.

Next, liquid toluene (Sigma-Aldrich, > 99.9 %) was injected with a syringe through a septum into a 6 mm stainless-steel tube, where it mixed with purified air, flowing into the chamber at the flow rate of $100 \, L \, min^{-1}$. The high flow rate was used to enhance the evaporation of the toluene. In the seeded experiments, we also injected liquid butanol-d9 into the chamber. The butanol-d9 is used as an OH radical tracer to determine the OH radical concentration (Barmet et al., 2012).

The concentrations of toluene, butanol-d9, and the oxidation products were monitored using a high-resolution proton transfer reaction mass spectrometer (PTR-TOF 8000, Ionicon Analytik, Innsbruck, Austria). Sample air from the chamber stainless-steel inlet port was introduced to the PTR drift tube via a 1.5 m long heated (60 °C) PEEK tubing (inner diameter 1 mm) at a flow rate of $160 \, mL \, min^{-1}$. Hydronium ions (H_3O^+) were used as a reagent to ionize organic compounds. PTR-MS was operated under controlled conditions (2.3 mbar drift tube pressure, 600 V drift tube voltage and 60 °C temperature). The raw PTR-MS data were post-processed by the PTR-MS Viewer 3.1.0.18 program (Ionicon Analytic). Concentrations in parts per billion (ppb) were calculated by the program using a standard reaction rate constant of $2 \times 10^{-9} \, cm^3 \, molecule^{-1} \, s^{-1}$.

After stabilization and mixing of the components, the blacklights were switched on. During the irradiation HONO efficiently photolyzes to form OH and NO. The initial OH radical concentration was estimated from the first-order decay of toluene observed in the PTR-MS. A reaction rate constant of $5.6 \times 10^{-12} \, cm^3 \, molecule^{-1} \, s^{-1}$ was used for the OH–toluene reaction (Calvert et al., 2002). It must be noted that OH radical formation through the HONO photochemistry produces easily a high concentration of NO, which is known to suppress SOA formation (Ng et al., 2007). If the presence of NO needs to be avoided, a different generation method for OH radicals, such as the photochemical decomposition of hydrogen peroxide (H_2O_2), should be used. However, we decided to use the HONO as an OH radical source, because NO_x is always present in combustion aerosol experiments, for which our chamber is designed.

The concentration of selected reaction products of toluene with OH were monitored with the PTR-MS. The selected reaction products were CH_3O^+ (m/z 31.018), $C_2H_5O^+$ (m/z 45.034), $C_3H_7O^+$ (m/z 59.049), $C_3H_5O_2^+$ (m/z 73.029), $C_4H_5O_2^+$ (m/z 85.029), $C_4H_3O_3^+$ (m/z 99.008), $C_5H_7O_2^+$ (m/z 99.044), $C_7H_7O^+$ (m/z 107.049), $C_7H_9O^+$ (m/z 109.065), $C_5H_5O_3^+$ (m/z 113.023), $C_7H_7O_2^+$ (m/z 123.045), $C_7H_9O_2^+$ (m/z 125.060), $C_6H_6NO_3^+$ (m/z 140.035), and $C_7H_8NO_3^+$ (m/z 154.050). They were selected based on toluene photooxidation reactions provided by the Master Chemical Mechanism (MCMv3) model (Wagner et al., 2003; Gómes Alvarez et al., 2007). Molar yields of gas phase oxidation products were calculated as the slope of the linear regression between the amounts of the product and of reacted toluene. Possible secondary reactions with ozone and OH radicals, appearing as decreasing concentrations of the products after the initial maximum, were not included in the yield calculations.

The SOA yield, Y, was calculated as the ratio of the formed mass, ΔM_o ($\mu g \, m^{-3}$), to the reacted toluene (a volatile organic compound, VOC) mass, ΔVOC ($\mu g \, m^{-3}$), in the course of the experiment, as

$$Y = \Delta M_o / \Delta VOC. \tag{3}$$

The formed mass was estimated from the size-dependent, wall-loss-corrected total aerosol volume, calculated from the
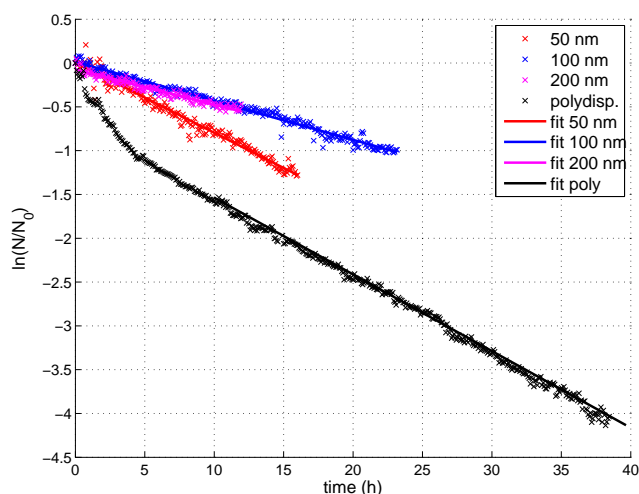
Figure 3. The logarithmic relative number concentration as a function of time of 50, 100, and 200 nm monodisperse and polydisperse ammonium sulfate aerosols. The equations for the linear fittings are $\ln(N/N_0) = -0.0803t + 0.0078$ (50 nm), $\ln(N/N_0) = -0.0445t + 0.0128$ (100 nm), $\ln(N/N_0) = -0.0403t - 0.0722$ (200 nm), and $\ln(N/N_0) = -0.0875t + 0.8878$ (polydisperse, after 10 h).

SMPS data, and by assuming a density of 1400 kg m^{-3} for the produced SOA (Ng et al., 2007).

3 Results

3.1 Particle wall loss rates

The particle wall loss rate constants in Eq. (1) for 50, 100, and 200 nm monodisperse particles ($\beta_{50 \text{ nm}}$, $\beta_{100 \text{ nm}}$, and $\beta_{200 \text{ nm}}$) with an initial number concentration of 1690, 840, and 340 cm^{-3}, were 0.080, 0.045, and 0.040 h^{-1}, respectively (Fig. 3). In order to obtain the β_i for all particle size classes i we fitted a second-order polynomial to the data (log $d_{p,j}$, β_j), where $d_{p,j}$ is the monodisperse particle size.

The wall loss rates in the Ilmari chamber are only 18–33 % of those observed by Wang et al. (2014) in a 30 m^3 chamber. One possible reason for the difference is that the chamber in Ilmari has no mixing fans which could enhance the wall deposition by increasing turbulence inside the chamber. Furthermore, Wang et al. (2014) used excerpts of polydisperse aerosol, while our rates were determined for almost-pure monodisperse aerosol (including up to 27 % of larger, multiply charged particles), for which the coagulation rate is smaller than for polydisperse aerosols with the same number concentration (e.g., Seinfeld and Pandis, 2006). Also, at the number concentrations in our experiments the effect of coagulation is only minor or negligible at the timescales of our experiments (maximum duration 40 h), as discussed, e.g., by Cocker et al. (2001).

The wall loss rate for polydisperse aerosol was faster in the beginning and levelled off to 0.088 h^{-1} in 10 h (Fig. 3).
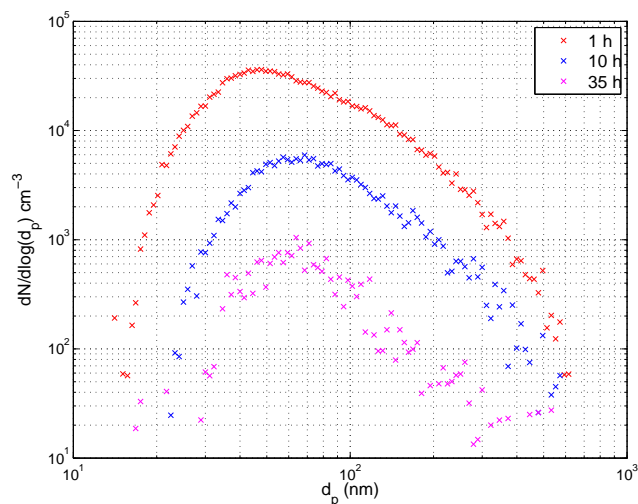

Figure 4. The size distribution of the polydisperse ammonium sulfate aerosol 1, 10, and 35 h after injecting the aerosol into the chamber.

In the beginning of the experiment the particle number concentration was $12\,700 \text{ cm}^{-3}$, so coagulation has more significance in reducing the number concentration. Also, smaller particles deposit faster onto the chamber walls. Figure 4 illustrates these effects: the median of the particle size increases from the initial 50 to 65 nm in 10 h. After this, no growth of particles but only decrease in concentration is observed.

The polydisperse aerosol number loss rate in our chamber is comparable to those in, e.g., the Guangzhou (30 m^3), Paul Scherrer Institute (PSI, 27 m^3), and California Institute of Technology (28 m^3) chambers with loss rates of 0.17 h^{-1}, $0.209 \pm 0.018 \text{ h}^{-1}$, and $0.09\text{–}0.18 \text{ h}^{-1}$, respectively (Wang et al., 2014; Paulsen et al., 2005; Cocker et al., 2001). The particle half-life in our chamber is 8–17 h, which is remarkably longer than, e.g., the $2.8 \pm 0.8 \text{ h}$ in the PSI mobile chamber (Platt et al., 2013). The longer half-life arises from a smaller surface-to-volume ratio, which is 2.0 m^{-1} in our chamber, as compared to 3.0 m^{-1} in the PSI mobile chamber. Also, as can be seen in our measurements, the loss rate is highly dependent on particle size, and the overall decrease rate of the total number concentration depends on the size distribution of the inspected aerosol, which makes an exact comparison difficult.

3.2 Blacklight lamps and NO_2 photolysis rate

Irradiation wavelengths of the 365 and 350 nm lamps are 340–400 nm and 310–400 nm, respectively. The irradiation wavelength of the 365 nm lamps is similar to many important photochemical reactions, such as NO_2 photolysis and OH radical formation from HONO, but some atmospherically relevant reactions are slow or non-existent compared to their atmospheric rates because of the low or missing 310–340 nm irradiation (Seinfeld and Pandis, 2006). These reac-

tions include O_3 photolysis to O^1D and its further forming of OH radicals, and photolysis of aldehydes and ketones. The photolysis of these simple carbonyls can directly produce alkoxy radicals that react quickly with O_2 to form more HO_2 radicals. In high-NO_x experiments this can increase important OH radical production by converting HO_2 to OH when HO_2 reacts with NO.

For the 365 and 350 nm lamps, there is no irradiation in the visible light region above 400 nm. This region would be important especially for α-dicarbonyl (e.g., glyoxal and methylglyoxal) photolysis and their following radical reactions. The same compounds have also been confirmed as products of toluene photooxidation. Missing the visible light region in toluene chamber experiments might have some effect on gas phase oxidation product yields and also SOA formation.

The integral irradiances over the wavelengths of 340–400 nm with the set of one-third, two-thirds, and all of the 365 nm blacklights switched on were 9.7, 19.7, and 29.3 W m^{-2}, respectively. The integral irradiance over the same wavelength range in Kuopio at noon in July in sunny and cloudy weather was 20.2 and 8.7 W m^{-2}, respectively, so by switching a selected number of blacklights on we can reproduce an irradiance comparable to the outdoor conditions in the wavelength range of the blacklights. However, it must be noted that the irradiance spectrum of the blacklights is very narrow compared to the solar irradiance spectrum (Fig. 2).

The NO_2 photolysis rate (Eq. 2) for the 365 nm lamps at 9.8, 14.7, and 29.7 W m^{-2} irradiances were 0.0037, 0.0058, and 0.0103 s^{-1} (or 0.22, 0.35, and 0.62 min^{-1} or 13.2, 20.8, and 37.1 h^{-1}), respectively. For the 350 nm lamps, the NO_2 photolysis rate with all lamps on was 0.0022 s^{-1} (or 0.132 min^{-1} or 7.9 h^{-1}). The correction due to dark reactions of ozone and NO in the sampling line was less than 1.4 % for each compound and irradiance. The maximum NO_2 photolysis rate in our chamber is comparable to those reported in other indoor photoreactors, such as 0.12 min^{-1} in the 27 m^3 chamber at the Paul Scherrer Institute (Paulsen et al., 2005); 0.19 min^{-1} in the 90 m^3 environmental chamber at the University of California, Riverside (Carter et al., 2005); 1.5 min^{-1} in the 28 m^3 chamber at the California Institute of Technology (Cocker et al., 2001); and $8.0 \pm 0.7 \times 10^{-3}$ s^{-1} in the mobile environmental chamber of PSI (Platt et al., 2013).

3.3 Temperature control and distribution

The air conditioning is capable of keeping the temperature below 25 and within 1 °C. This is important because the equilibria of the semivolatile species between the gas and particle phase are usually exponentially temperature-dependent. Furthermore, condensation in the sampling lines is possible when a warmer sample enters colder sampling lines, at least in experiments with a high relative humidity in the chamber.
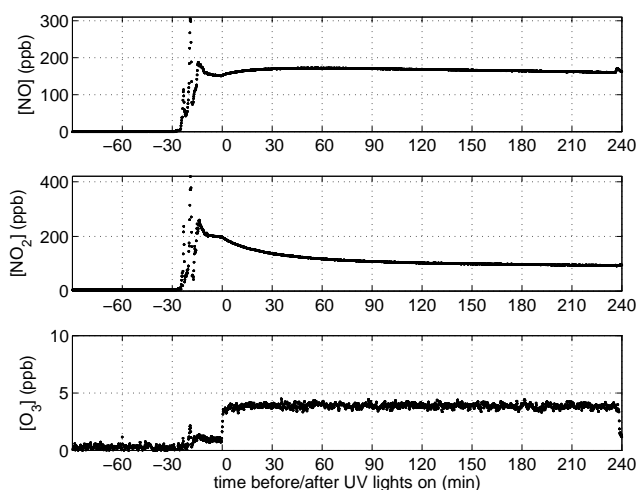

Figure 5. The evolution of **(a)** NO, **(b)** NO_2, and **(c)** O_3 concentrations in the chamber in experiment T150113. Seed particle injection started at -86 min and ended at -81 min; toluene and butanol-d9 were injected at -61 and -57 min, respectively; and HONO injection started at -30 min and ended at -23 min. The blacklights were on for the time period of 0–238 min.

The temperature inside the chamber was quite uniformly distributed. When the lights were off, the temperatures in each corner were within 0.5 °C. The difference was greater when the lights were on, being 0.9 °C at maximum. The differences are unlikely to cause, e.g., thermal diffusion in a certain direction, or thermophoretic effects.

3.4 SOA formation experiments

In the blank experiments with pure air the wall-loss-corrected particle mass concentration after 4 h of irradiation was 0.5–2.5 µg m^{-3}. The background aerosol concentration is at the same level as that observed by Carter et al. (2005) in a new chamber. In the experiments with pure air and CO the wall-loss-corrected mass concentration after 4 h of irradiation was 0.3 µg m^{-3}. This observation is also in accordance with the results of Carter et al. (2005). This means that no – or very little – aerosol off-gassing from the chamber walls is observed but that the background particle formation is due to particle precursors originating from the purified air source or off-gassing of NO_x and other reactive gases, such as HONO or formaldehyde, from the chamber walls. The NO_x off-gassing may contribute, e.g., to ozone yields in the presence of hydrocarbons. The HONO released from the chamber walls, in turn, photolyzes rapidly to NO and OH radicals, which may have an effect on SOA formation.

The initial concentrations of ozone, HONO, toluene, and NO_x in the chamber in the toluene irradiation experiments are given in Table 1. The NO_x in the chamber originates mostly from the injected HONO, because the concentrations

Table 1. Initial concentrations and conditions in the test runs with toluene. N/A: the data are missing due to problems in PTR-MS.

Run	[O_3] (ppb)	[NO_2]$_{HONO}$ (ppb)	[Toluene] (ppb)	[NO_x] (ppb)	[OH]$\times 10^7$ (cm^{-3})	T (°C)	RH (%)	N (cm^{-3})
T130909	48.5	18.8	24.7	19.1	2.3	22.2	54.0	N/A
T130910	53.8	20.1	25.3	22.4	2.1	20.4	65.0	56
T130911	55.2	12.6	26.2	11.9	1.5	22.6	67.9	44
T130912	29.8	128.4	18.2	131.2	N/A	19.3	79.2	10
T150113	2.1	197.2	29.9	349.0	2.1	19.7	46.8	10 375
T150114	3.1	432.7	29.4	577.7	3.8	18.4	51.4	16 180
T150120	1.9	371.2	28.8	624.4	2.4	18.9	55.1	13 215
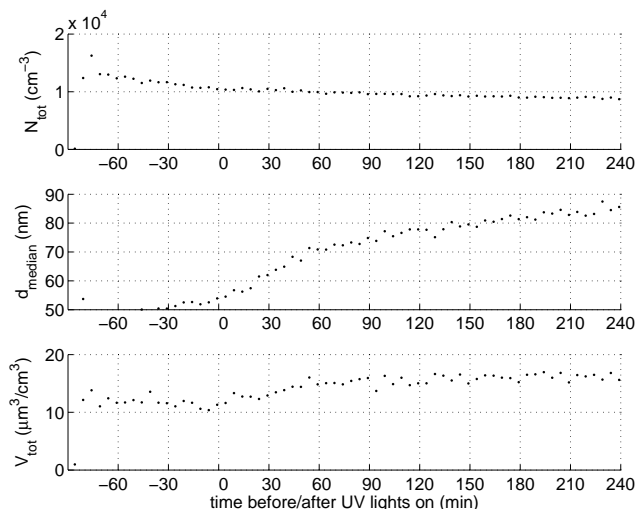
Figure 6. The evolution of **(a)** aerosol number concentration, **(b)** median diameter, and **(c)** calculated volume concentration (corrected for wall losses) in the chamber in experiment T150113. Seed particle injection started at −86 min and ended at −81 min; toluene and butanol-d9 were injected at −61 and −57 min, respectively; and HONO injection started at −30 min and ended at −23 min. The blacklights were on for the time period of 0–238 min.

of both NO and NO_2 were less than 0.6 ppb before injecting HONO in each experiment.

After switching the blacklights on, the NO from the decomposition of HONO was converted rapidly into NO_2 because there was always ozone present in the chamber. The NO_2 decomposed into NO and O, which, in turn, produced ozone. There was a net production of ozone, and the ozone was seen to accumulate into the chamber. For example, the maximum ozone concentration was 4.5 ppb in experiment T150113 (Fig. 5).

The SOA volume (and mass) increased under the influence of UV radiation (Fig. 6). In experiments without seed particles, the SOA particles were detected when they had grown to larger than 14 nm in diameter, the lower detection limit of the SMPS. This took place approximately 10 min after the lights had been switched on. Over time, the SOA volume concentrations levelled off and reached 11.8, 10.2, and 5.0 µm^3 cm^{-3} in 295, 195, and 93 min in the experiments

T130910, T130911, and T130912, respectively. In experiments T150113, T150114, and T150120, with seed particles, the aerosol volume concentration increased by 4.0, 7.6, and 4.0 µm^3 cm^{-3} during 240 min, respectively. The corresponding SOA mass concentrations, toluene consumption, and the SOA yields, calculated by using Eq. (3), are given in Table 2.

The SOA yields in the seeded experiments were 0.12 when j_{NO_2} was 0.13 min^{-1} and 0.18 when j_{NO_2} was 0.28 min^{-1} (Table 2). These are comparable to the yields of 0.08–0.13 obtained by Ng et al. (2007) in seeded, high-NO_x experiments. In the unseeded experiments, the SOA yields were 0.33–0.42, even though the SOA yield is known to be lower without seed particles (Kroll et al., 2007), because more of the vapors are lost to the chamber walls in the absence of seed particles (Zhang et al., 2014; Kokkola et al., 2014). However, NO_x concentration in the seeded experiments was remarkably higher than in the unseeded ($j_{NO_2} = 0.28$ min^{-1}) experiments, and NO_x is known to suppress SOA formation (Ng et al., 2007). Huang et al. (2013) obtained a SOA yield of approximately 0.1 when no seed particles were present and 0.2–0.4 when seed particles were present, depending on the seed particle material. It must be noted that Ng et al., 2007; Kroll et al. (2007) and Huang et al. (2013) carried out their experiments in dry conditions (RH 4–7 % or 15 %), while in our experiments RH was 54–79 %. This may have enhanced the SOA yields, because a higher humidity is known to increase the SOA yield remarkably (Zhou et al., 2011; Keller and Burtscher, 2012).

As the above discussion indicates, the comparison of yields between different laboratories and facilities is quite complicated because there are many factors (at least seed/no seed, low/high NO_x, HC / NO_x ratio, light intensity and wavelength range, humidity, vapor wall losses, aerosol wall loss corrections) that have an effect on the calculated yield values. It must be noted that also the background particle precursors have their contribution to the SOA yield. For example, in our toluene experiments the background concentration of up to 1.9 µg m^{-3} corresponds to 11–34 % of the formed SOA in our experiments, which is definitely not negligible. However, the background concentration varies from experiment to experiment and cannot be measured for each experiment separately, which makes the yield calculation and comparison even more complicated.

Table 2. Lamps used, formed SOA mass (ΔM_o), reacted toluene mass (ΔVOC), and SOA yield (Y) in the test runs with toluene. N/A: the data are missing due to problems in SMPS.

Run	Lamps	j_{NO_2} (min^{-1})	ΔM_o (µg m^{-3})	ΔVOC (µg m^{-3})	Y
T130909	365 nm	0.28	N/A	28.8	N/A
T130910	365 nm	0.28	16.6	39.7	0.42
T130911	365 nm	0.28	14.3	39.3	0.36
T130912	365 nm	0.28	7.0	21.1	0.33
T150113	350 nm	0.13	5.6	45.2	0.12
T150114	365 nm	0.28	10.6	59.1	0.18
T150120	350 nm	0.13	5.7	47.4	0.12

Table 3. Gas phase oxidation product yields from oxidation of toluene on percent basis. N/A: the data are missing due to problems in PTR-MS.

Run	m/z 31.018	m/z 45.034	m/z 59.049	m/z 73.029	m/z 85.029	m/z 99.008	m/z 99.044	m/z 107.049	m/z 109.065
T130909	5.5	14.6	11.8	5.3	0.5	1.3	9.5	7.5	7.2
T130910	6.4	18.3	11.3	15.4	4.1	2.7	14.4	7.8	8.6
T130911	5.9	22.5	13.7	19.5	7.6	7.6	19.5	8.4	9.3
T130912	N/A	N/A	N/A	N/A	N/A	N/A	N/A	N/A	N/A
T150113	5.8	N/A	2.5	14.6	11.5	11.5	15.3	8.9	14.2
T150114	6.0	11.6	1.8	13.7	9.0	12.7	12.4	7.5	9.5
T150120	6.0	11.5	4.4	12.8	6.6	7.9	5.8	8.2	11.8

Time evolution of toluene and selected reaction product ion concentrations in experiment T150113 are illustrated in Fig. 7. The main toluene photooxidation products are organized according to the four reaction paths described by Wagner et al. (2003). The major reaction mechanism, named the dicarbonyl route, includes OH addition to the aromatic ring as a first reaction step, which is followed by cleavage of the ring. In our results, the ions m/z 73.029 (e.g., methylglyoxal), m/z 85.029 (e.g., 2-butenedial or 2(5H)-furanone) and m/z 99.044 (e.g., 4-oxo-2-pentenal) can be identified as first-generation oxidation products due to their rapid concentration increase in the beginning of the experiment. Of these, the concentrations of the ions m/z 85.029 and m/z 99.044 decrease after 30 min of UV irradiation as their consumption exceeds their production (Fig. 7a).

Furthermore, in accordance with the reaction pathway described by Wagner et al. (2003), the formation of the second-generation oxidation products with m/z 99.008 (e.g., 2,5-furandione) and m/z 113.023 (e.g., methyl-2,5-furandione) can be observed in our results. Their concentrations increase slowly during the entire duration of 240 min UV exposure (Fig. 7a). The detailed formation mechanism of these OH-radical-initiated oxidation products of toluene have been further discussed in earlier studies (e.g., Forstner et al., 1997; Wagner et al., 2003; Gómes Alvarez et al., 2007). However, unlike Wagner et al. (2003) suggest, we did not find clear experimental evidence for the epoxide route as the first-generation reaction product 2,3-epoxy-6-oxo-4-heptenal was not detected. Still, the epoxide route compounds can be fur-

ther oxidized, and they can form reaction products similar to the detected dicarbonyl route.

Moreover, the two remaining major reaction routes starting with cresol (m/z 109.065) and benzaldehyde (m/z 107.049) were clearly distinguished as the formation of their first-generation reaction products increased rapidly after the UV lights were switched on (Figs. 7b and c). We were also able to detect some of the possible secondary oxidation products from both oxidation routes. Methyl nitrophenol (m/z 154.050) and nitrophenol (m/z 140.035) are second-generation products from cresol route and benzaldehyde route, respectively (Wagner et al., 2003). Finally, we measured only a weak formation of benzoquinones (Fig. 7d), which is again in line with Wagner et al. (2003) model results.

The yields for the selected gas phase oxidation products in toluene photooxidation experiments are given in Tables 3 and 4. Similarly to other studies (Smith et al., 1998; Wagner et al., 2003; Gómes Alvarez et al., 2007), the highest formation yields in the current study were detected in the compounds representing the dicarbonyl route and the cresol route. The highest formation yields were detected for m/z 73.029 (12.8–19.5 %) and m/z 99.044 (5.8–19.5 %) ions, which have the same molecular composition as methyl glyoxal and 4-oxo-2-pentenal, respectively. Smith et al. (1998) and Gómes Alvarez et al. (2007) observed comparable yields of 16.7–37.0 % for methyl glyoxal and 3.1–13.8 % for 4-oxo-2-pentenal. Furthermore, Gómes Alvarez et al. (2007) measured a yield of 13 % for 2-butenedial, which is comparable to that of the ion with m/z 85.029 (4.1–11.5 %) in our

Table 4. Yields of selected gas phase oxidation products of toluene on percent basis in experiments T150113, T150114, and T150120.

Run	m/z 113.023	m/z 123.045	m/z 125.060	m/z 140.035	m/z 154.050
T150113	1.1	0.9	0.5	0.3	0.4
T150114	1.2	0.8	0.3	0.5	0.4
T150120	0.7	0.8	0.2	0.2	0.1
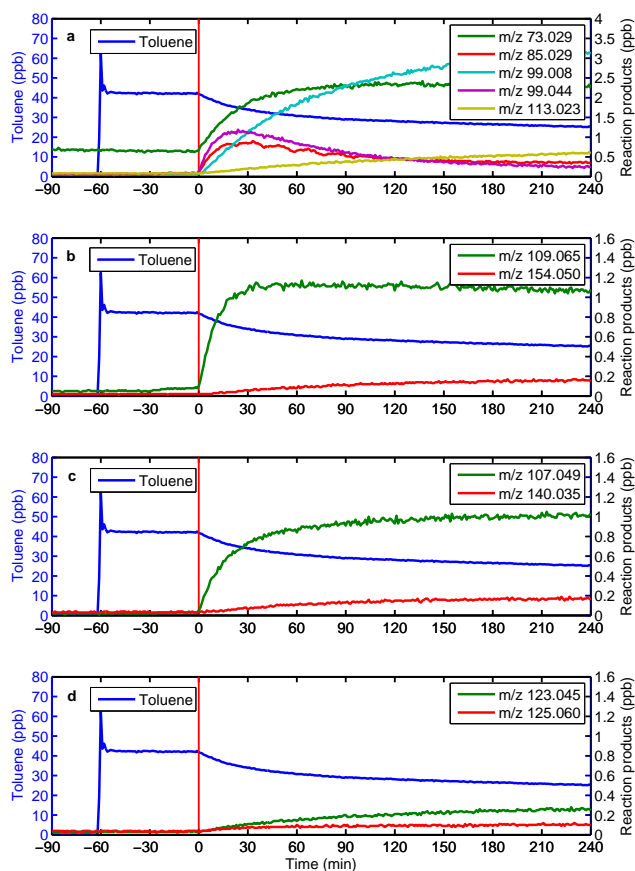
Figure 7. The evolution of the concentrations of toluene and selected oxidation products in toluene photooxidation experiment T150113. The major reaction products are organized according to the addition of OH and following ring-opening or retaining reaction routes or H-abstraction route: **(a)** dicarbonyl route, **(b)** cresol route, **(c)** benzaldehyde route, and **(d)** quinone route. Tentatively identified reaction products: m/z 73.029 (e.g., methyl glyoxal), m/z 85.029 (e.g., 2-butenedial), m/z 99.008 (e.g., 2,5-furandione), m/z 99.044 (e.g., 4-oxo-2-pentenal), m/z 107.049 (e.g., benzaldehyde), m/z 109.065 (e.g., cresol), m/z 113.023 (e.g., 3-methyl-2,5-furandione), m/z 123.045 (e.g., 2-methyl-1,4-benzoquinone), m/z 125.060 (e.g., 2-methyl-1,4-benzenediol), m/z 140.035 (e.g., nitrophenol), and m/z 154.050 (e.g., methyl nitrophenol).

measurements. Smith et al. (1998) reported a similar yield for benzaldehyde (6 %) but almost a double yield for cresol (17.9 %) compared to this study. The slight variations in our observed yields are at least in part explained by the differ-

ences in the initial conditions of the chamber experiments, such as varying initial concentrations of NO_x or HONO.

Glyoxal (m/z 59.013) has been confirmed as one of the main photooxidation products of toluene (e.g., Smith et al., 1998). In the first set of the experiments (T130909–130911) we could not identify glyoxal with PTR-MS because the signal interfered with the near peak for acetone (m/z 59.049). In the second set of experiments (T150113, T150114, T150120) we detected only low levels of glyoxal formation (product yield < 1 %). The formation was clearly smaller than those reported in earlier toluene photooxidation studies with yields of 23.8–37.0 % (Smith et al., 1998; Gómes Alvarez et al., 2007). Our smaller glyoxal yields could be explained by differences in the experimental conditions or in the PTR measurement sensitivity. Glyoxal has a proton affinity of 161–165 kcal mol^{-1} (Wróblewski et al., 2007), which is almost the same as that of water (166 kcal mol^{-1}). Because the proton affinity of glyoxal is so close to that of water, a reverse proton transfer reaction likely happens in the PTR drift tube, which results in evidently less efficient detection of glyoxal (Gouw and Warneke, 2007).

The oxidation products of toluene can be found in both gaseous and particulate phases, as reported by earlier research (Forstner et al., 1997; Sato et al., 2007; White et al., 2014). Our analysis did not include a detailed chemical analysis of the particulate phase, and therefore the yields in Tables 3 and 4 could be underestimations.

4 Conclusions

The functionality of the new environmental chamber at the Ilmari research facility was tested for secondary product formation both in particle and gas phase. The observed yields of SOA and gaseous first- and second-generation reaction products were reasonable and comparable to those obtained in other laboratories. However, a direct comparison is challenging because the yields depend greatly on conditions and initial concentrations. For quantitative verification of the yields, calculations with a photooxidation reaction model, such as the MCM, would be needed.

The wall loss rates of aerosol particles on the chamber walls are small enough, because of the low surface-to-volume ratio, to enable experiments with duration of several hours. The particle half-life in the chamber at Ilmari is comparable to or somewhat longer than those in other laboratories. The movable top of the chamber enables maintaining an

overpressure in the chamber during the experiments, which prevents dilution of the sample in the chamber and contaminants from entering the chamber.

References

Barmet, P., Dommen, J., DeCarlo, P. F., Tritscher, T., Praplan, A. P., Platt, S. M., Prévôt, A. S. H., Donahue, N. M., and Baltensperger, U.: OH clock determination by proton transfer mass spectrometry at an environmental chamber, Atmos. Meas. Tech., 5, 647–656, doi:10.5194/amt-5-647-2012, 2012.

Calvert, J. G., Atkinson, R., Becker, K. H., Kamens, R. M., Seinfeld, J. H.,Wallington, T. J., and Yarwoord, G.: The Mechanisms of Atmospheric Oxidation of Aromatic Hydrocarbons, Oxford University Press, New York, 556 pp., 2002.

Carter, W. P. L., Cocker, D. R. III, Fitz, D. R., Malkina, I. L., Bumiller, K., Sauer, C. G., Pisano, J. T., Bufalino, C., and Song, C.: A new environmental chamber for evaluation of gas-phase chemical mechanisms and secondary aerosol formation, Atmos. Environ., 39, 7768–7788, doi:10.1016/j.atmosenv.2005.08.040, 2005.

Cocker, D. R. III, Flagan, R. C., and Seinfeld, J. H.: State-of-the-art chamber facility for studying atmospheric aerosol chemistry, Environ. Sci. Technol., 35, 2594–2601, 2001.

Crump, J. G., Flagan, R. C., and Seinfeld, J. H.: Particle wall loss rates in vessels, Aerosol Sci. Technol., 2, 303–309, 1983.

Forstner, H. J., Flagan, R. C., and Seinfeld, J. H.: Secondary organic aerosol from the photooxidation of aromatic hydrocarbons: molecular composition, Environ. Sci. Technol., 31, 1345–1358, 1997.

Gómes Alvarez, E., Viidanoja, J., Muños, A., Wirtz, K., and Hjorth, J.: Experimental Confirmation of the Dicarbonyl Route in the Photo-oxidation of Toluene and Benzene, Environ. Sci. Technol., 41, 8362–8369, 2007.

Gouw, J. and Warneke, C.: Measurement of volatile organic compounds in the earth's atmosphere using proton-transfer-reaction mass spectrometry, Mass Spectrom. Rev., 26, 223–257, 2007.

Hallquist, M., Wenger, J. C., Baltensperger, U., Rudich, Y., Simpson, D., Claeys, M., Dommen, J., Donahue, N. M., George, C., Goldstein, A. H., Hamilton, J. F., Herrmann, H., Hoffmann, T., Iinuma, Y., Jang, M., Jenkin, M. E., Jimenez, J. L., Kiendler-Scharr, A., Maenhaut, W., McFiggans, G., Mentel, Th. F., Monod, a., Prévôt, A. S. H., Seinfeld, J. H., Surratt, J. D., Szmigielski, R., and Wildt, J.: The formation, properties and impact of secondary organic aerosol: current and emerging issues,

Atmos. Chem. Phys., 9, 5155–5236, doi:10.5194/acp-9-5155-2009, 2009.

Huang, M., Hao, L., Gu, X., Hu, C., Zhao, W., Wang, Z., Fang, L., and Zhang, W.: Effects of inorganic seed aerosols on the growth and chemical composition of secondary organic aerosol formed from OH-initiated oxidation of toluene, J. Atmos. Chem., 70, 151–164, doi:10.1007/s10874-013-9262-9, 2013.

Keller, A. and Burtscher, H.: A continuous photo-oxidation flow reactor for a defined measurement of the SOA formation potential of wood burning emissions, J. Aerosol Sci., 49, 9–20, doi:10.1016/j.jaerosci.2012.02.007, 2012.

Kokkola, H., Yli-Pirilä, P., Vesterinen, M., Korhonen, H., Keskinen, H., Romakkaniemi, S., Hao, L., Kortelainen, A., Joutsensaari, J., Worsnop, D. R., Virtanen, A., and Lehtinen, K. E. J.: The role of low volatile organics on secondary organic aerosol formation, Atmos. Chem. Phys., 14, 1689–1700, doi:10.5194/acp-14-1689-2014, 2014.

Kroll, J. H., Chan, A. W. H., Ng, N. L., Flagan, R. C., and Seinfeld, J. H.: Reactions of semivolatile organics and their effects on secondary organic aerosol formation, Environ. Sci. Technol., 41, 3545–3550, doi:10.1021/es062059x, 2007.

Lambe, A. T., Ahern, A. T., Williams, L. R., Slowik, J. G., Wong, J. P. S., Abbatt, J. P. D., Brune, W. H., Ng, N. L., Wright, J. P., Croasdale, D. R., Worsnop, D. R., Davidovits, P., and Onasch, T. B.: Characterization of aerosol photooxidation flow reactors: heterogeneous oxidation, secondary organic aerosol formation and cloud condensation nuclei activity measurements, Atmos. Meas. Tech., 4, 445–461, doi:10.5194/amt-4-445-2011, 2011.

McMurry, P. H. and Grosjean, D.: Gas and aerosol wall losses in teflon film smog chambers, Environ. Sci. Technol., 19, 1176–1182, 1985.

Ng, N. L., Kroll, J. H., Chan, A. W. H., Chhabra, P. S., Flagan, R. C., and Seinfeld, J. H.: Secondary organic aerosol formation from m-xylene, toluene, and benzene, Atmos. Chem. Phys., 7, 3909–3922, doi:10.5194/acp-7-3909-2007, 2007.

Paulsen, D., Dommen, J., Kalberer, M., Prévôt, A. S. H., Richter, R., Sax, M., Steinbachner, M., Weingartner, E., and Baltensperger, U.: Secondary organic aerosol formation by irradiation of 1,3,5-trimethylbenzene–NO_x–H_2O in a new reaction chamber for atmospheric chemistry and physics, Environ. Sci. Technol., 39, 2668–2678, 2005.

Platt, S. M., El Haddad, I., Zardini, A. A., Clairotte, M., Astorga, C., Wolf, R., Slowik, J. G., Temime-Roussel, B., Marchand, N., Ježek, I., Drinovec, L., Močnik, G., Möhler, O., Richter, R., Barmet, P., Bianchi, F., Baltensperger, U., and Prévôt, A. S. H.: Secondary organic aerosol formation from gasoline vehicle emissions in a new mobile environmental reaction chamber, Atmos. Chem. Phys., 13, 9141–9158, doi:10.5194/acp-13-9141-2013, 2013.

Sato, K., Hatakeyama, S., and Imamura T.: Secondary organic aerosol formation during the photooxidation of toluene: NO_x dependence of chemical composition, J. Phys. Chem. A, 111, 9796–9808, 2007.

Seinfeld, J. H. and Pandis, S. N.: Atmospheric Chemistry and Physics, edited by: Seinfeld, J. H. and Pandis, S. N., 204–283, Wiley, New York, 2006.

Smith, D. F., McIver, C. D., and Kleindienst, T. E.: Primary product distribution from the reaction of hydroxyl radicals with toluene at ppb NO_x mixing ratios, J. Atmos. Chem., 30, 209–228, 1998.

Taira, M. and Kanda, Y.: Continuous generation system for low-concentration gaseous nitrous acid, Anal. Chem., 62, 630–633, 1990.

Wagner, V., Jenkin, M. E., Saunders, S. M., Stanton, J., Wirtz, K., and Pilling, M. J.: Modelling of the photooxidation of toluene: conceptual ideas for validating detailed mechanisms, Atmos. Chem. Phys., 3, 89–106, doi:10.5194/acp-3-89-2003, 2003.

Wang, X., Liu, T., Bernard, F., Ding, X., Wen, S., Zhang, Y., Zhang, Z., He, Q., Lü, S., Chen, J., Saunders, S., and Yu, J.: Design and characterization of a smog chamber for studying gas-phase chemical mechanisms and aerosol formation, Atmos. Meas. Tech., 7, 301–313, doi:10.5194/amt-7-301-2014, 2014.

White, S. J., Jamie, I. M., and Angove, D. E.: Chemical characterisation of semi-volatile and aerosol compounds from the photooxidation of toluene and NO_x, Atmos. Environ., 83, 237–244, doi:10.1016/j.atmosenv.2013.11.023, 2014.

Wiedensohler, A.: An approximation of the bipolar charge distribution for particles in the submicron size range, J. Aerosol Sci., 19, 387–389, 1988.

Wróblewski, T., Ziemczonek, L., Alhasan, A. M., and Karwasz, G. P.: Ab initio and density functional theory calculations of proton affinities for volatile organic compounds, Eur. Phys. J. Special Topics, 144, 191–195, 2007.

Zhang, X., Cappa, C. D., Jathar, S. H., McVay, R. C., Ensberg, J. J., Kleeman, M. J., and Seinfeld, J. H.: Influence of vapor wall loss in laboratory chambers on yields of secondary organic aerosol, P. Natl. Acad. Sci. USA, published ahead of print April 7, 2014, 1–6, doi:10.1073/pnas.1404727111, 2014.

Zhou, Y., Zhang, H., Parikh, H. M., Chen, E. H., Rattanavaraha, W., Rosen, E. P., Wang, W., and Kamens, R. M.: Secondary organic aerosol formation from xylenes and mixtures of toluene and xylenes in an atmospheric urban hydrocarbon mixture: water and particle seed effects (II), Atmos. Environ., 45, 3882–3890, doi:10.1016/j.atmosenv.2010.12.048, 2011.

Ziemann, P. J. and Atkinson, R.: Kinetics, products, and mechanisms of secondary organic aerosol formation, Chem. Soc. Rev., 41, 6582–6605, doi:10.1039/c2cs35122f, 2012.